Inorganic Chemistry

pubs.acs.org/IC Article

Abundant Surface Defects in Cobalt Hydroxides/Oxyhydroxides Induced by Zinc Species Facilitate Water Oxidation

Shaojie Xu, Huijie Ni, Xiaodeng Zhang, Cheng Han, and Jinjie Qian*

Cite This: *Inorg. Chem.* 2023, 62, 14757−14763 Read Online

ABSTRACT: The complex process of the anodic oxygen evolution reaction (OER) severely hinders overall water splitting, which further limits the large-scale production and application of hydrogen energy. In this work, one type of bimetallic coordination polymer of ZnCoBTC using the MOF-on-MOF strategy has been synthesized where both Co(II) and Zn(II) cations exhibit the same coordination environment. By applying an electric potential, the predesigned bimetallic MOF precursor can be conveniently degraded into CoO_xH_y as an active species for efficient OER. Owing to the dissolution of ZnO_xH_y species, in situ formed disordered defects on the external surface of the catalyst increase the specific surface area as well as expose abundant active materials. Therefore, the $ZnCoO_xH_y$ nanosheet shows excellent OER performance and reaches an overpotential of only 334 mV at 10 mA cm^{-2} with a Tafel slope of 66.4 mV dec^{-1}, indicating fast reaction kinetics. The results demonstrate that metals with the same coordination environment can undergo in situ replacement or secondary growth on the pristine MOF, and they can be electrochemically degraded into highly efficient catalysts for future energy applications.

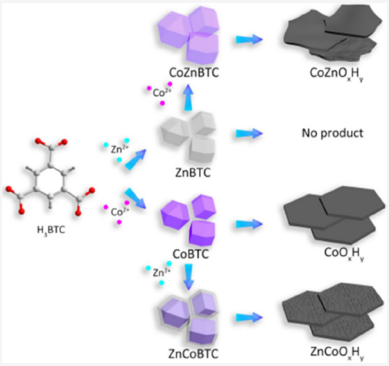

■ INTRODUCTION

The depletion of fossil fuels has become a pressing issue that necessitates collective action by human society. The development and implementation of renewable, clean energy are considered the most direct and effective approach to tackling this problem.[1,2] Hydrogen, with its exceptionally high combustion calorific value and absence of combustion byproducts that damage the environment, is regarded as one of the best clean energy sources.[3−56] Water electrolysis has been considered an efficient technique for hydrogen production, but the oxygen evolution reaction (OER) at the anode with a complex four-electron transfer process has posed a bottleneck in the overall water-splitting process.[7−9] Although commercial IrO_2 and RuO_2 are excellent catalysts for OER, their high cost and limited natural reserves have restricted their widespread use.[10−12] Consequently, researchers have progressively investigated the development and use of highly efficient, stable, and inexpensive OER catalysts for practical applications.

On the other hand, microporous metal−organic frameworks (MOFs) are formed by the self-assembly between metal cations and organic ligands and are deemed effective precursors or templates for OER catalysts.[13−1516] Due to their high specific surface area, large pore volume, and adjustable pore size, MOF materials and their derivatives have immense potential in gas storage and separation,[17,18] host−guest recognition,[19,20] electro/photocatalysis,[21−23] and more. As the coordination environments of different metals may be similar within isostructures, it is highly possible to rationally design and synthesize multimetal MOFs.[24−26] Furthermore, different metal sites in MOFs can exhibit different functions through appropriate treatment, enabling them to transform into highly active and stable catalytic nanomaterials.[27−293031] In recent years, there has been extensive research on MOF-derived transition metal species, which are considered to be ideal OER catalysts that can replace noble metal catalysts.[32−3435] Different types of metal derivatives play a crucial role, such as MOF-derived metal sulfides,[36] nitrides,[37,38] selenides,[39] phosphates,[40] and hydroxides,[41] which ensure effective resorption and desorption of reaction intermediates during catalysis, thereby reducing the energy required for OER reactions. However, the poor conductivity and small active area of metal hydroxides/oxyhydroxides limit their widespread use in OER.

In this work, we have prepared one type of bimetallic MBTC (BTC = benzene-1,3,5-tricarboxylate) using the same coordination environment of the metals Zn(II) and Co(II). The introduction of a second metal can competitively substitute the original metal in initial MOFs,[42,43] thereby creating the core−shell CoZnBTC and ZnCoBTC through secondary growth. The obtained bimetallic precursors are then transformed into $CoZnO_xH_y$ and $ZnCoO_xH_y$, which significantly improve the

Received: July 3, 2023
Published: August 28, 2023

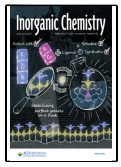

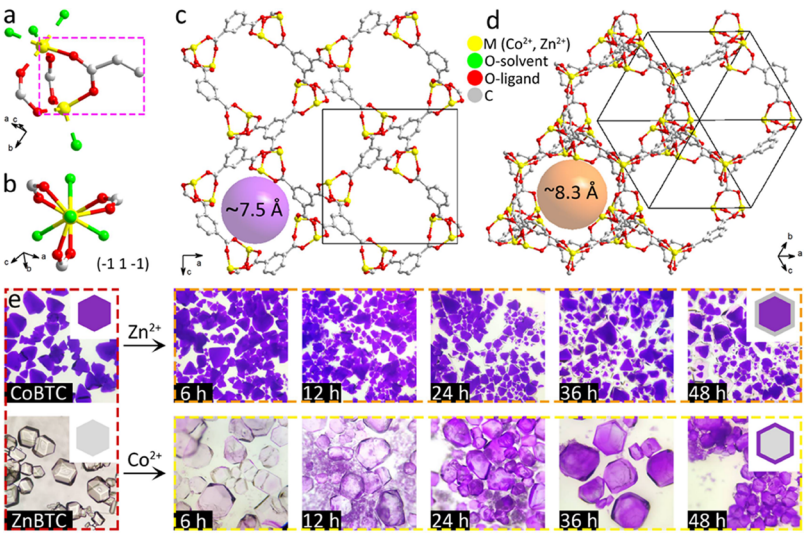

Figure 1. (a, b) AU and SBU and (c, d) two different channels of MBTC; and (e) Microscopic crystal morphologies of CoBTC and ZnBTC, and visualization of crystal growth over time.

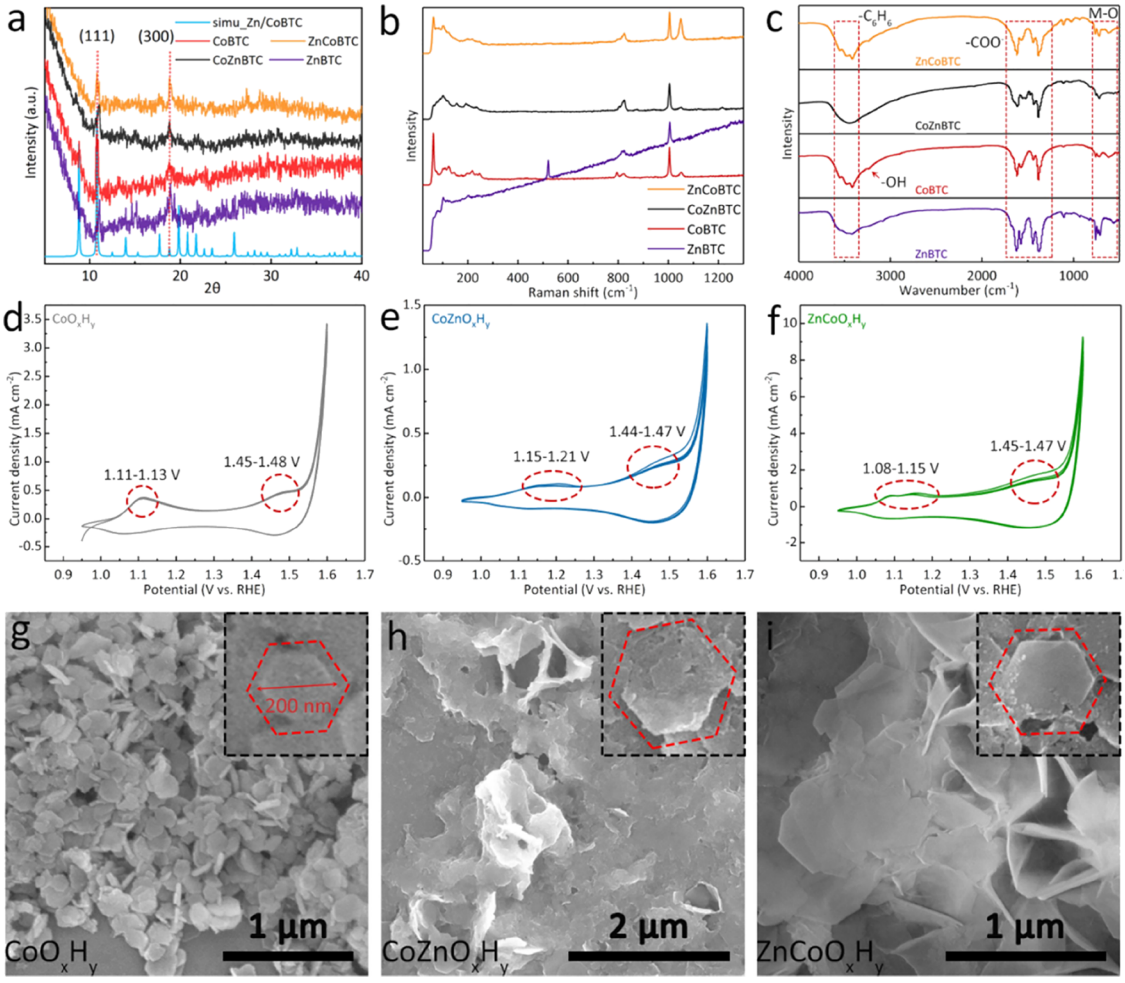

Figure 2. (a) PXRD patterns, (b) Raman spectra, and (c) FT-IR curves of MBTC; the stable CV curves of (d) CoO_xH_y, (e) $CoZnO_xH_y$, and (f) $ZnCoO_xH_y$ at 10 mV s^{-1} in 1.0 M KOH at 0.95−1.60 V.

electrical conductivity and mass transfer capacity. It is worth noting that ZnO_xH_y species are generated during electrochemical degradation and dissolve in the electrolyte simultaneously. Among them, the resulting $ZnCoO_xH_y$ catalyst shows a small overpotential of 334 mV, a Tafel slope of 62.6 mV dec^{-1}, and a high current retention rate of 97.8% after 10 h. This work demonstrates the possibility of synthesizing multimetal MOFs through rational coordination design and

https://doi.org/10.1021/acs.inorgchem.3c02210
Inorg. Chem. 2023, 62, 14757−14763

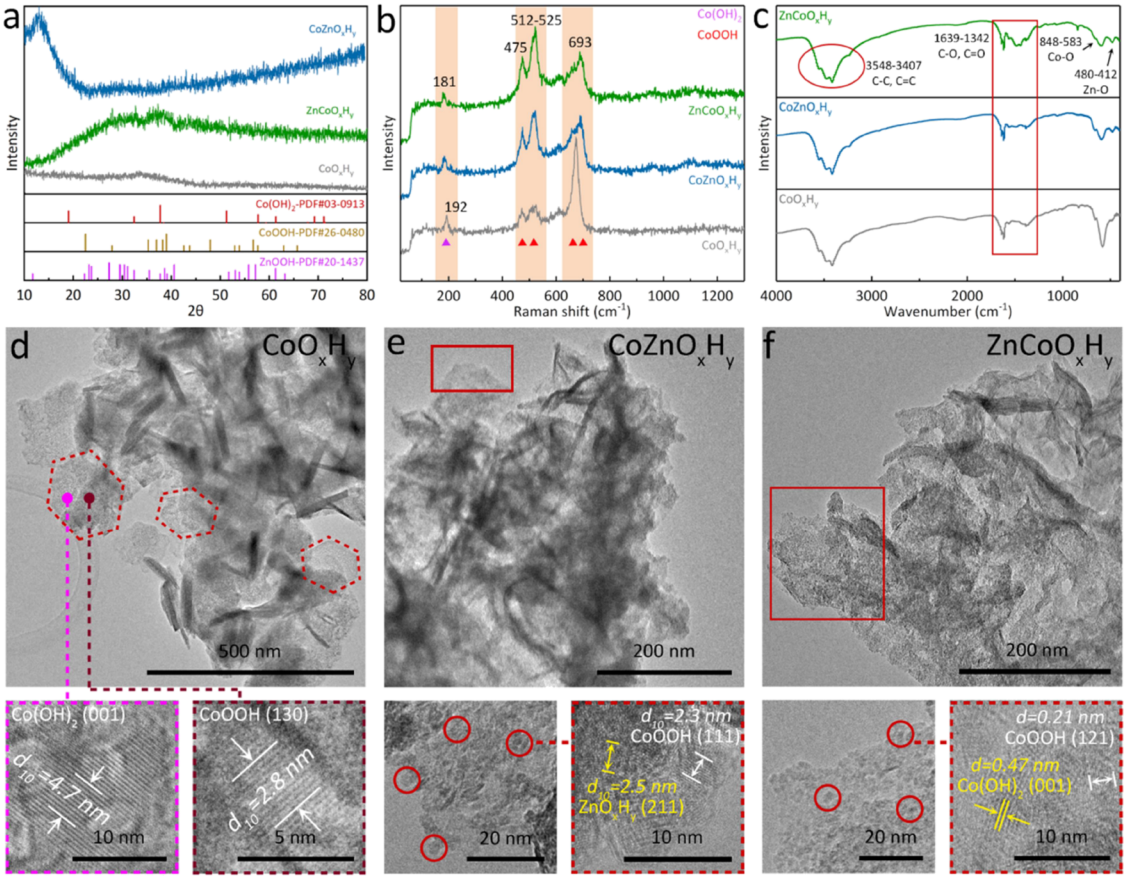

Figure 3. (a) PXRD patterns; (b) Raman spectra; and (c) FT-IR curves of CoO_xH_y, $CoZnO_xH_y$, and $ZnCoO_xH_y$; TEM images and lattice fringes of (d) CoO_xH_y; (e) $CoZnO_xH_y$; and (f) $ZnCoO_xH_y$.

obtaining high-efficiency OER catalysts for efficient energy storage and conversion applications.

The monometallic MBTC can be synthesized by heating a mixture of H_3BTC and a metal salt, where the secondary building unit (SBU) presents a paddle-wheel structure as shown in Figure 1a,b. The high symmetry of MBTC is confirmed by observing the asymmetric unit (AU) in the dashed purple region, where the three carboxylic acids exhibit consistent coordination environments along the (−11−1) crystal plane. The presence of water molecules at the ends of the metal centers leads to the existence of two different coordination modes, resulting in 1D tubular channels with a diameter of 7.5 Å along the three axes and another pore nanostructure with a size of 8.3 Å (Figures 1c,d, S1, and S2). However, the entrapment of solvents into the pores leads to a lower adsorption capacity and specific surface area (Figure S3). The two isostructures enable the successful growth of MOF-on-MOF heterostructures (Tables S2 and S3),[44] where $Zn(NO_3)_2$ is added to the synthetic CoBTC solution, and the thickness of the generated ZnBTC is visualized as a function of time (Figures 1e and S4). ZnBTC crystallizes on the surface of CoBTC easily under the action of the remaining H_3BTC and replaces Co in CoBTC to give bimetallic ZnCoBTC with a preserved morphology. To further prove the in situ released metal or ligand for binary MOF growth, the synthesized CoBTC gradually transforms from dark purple to colorless and transparent without H_3BTC, and the centrifuged ZnBTC shows a similar trend after the addition of Co(II) salt (Figure S5). The crystal structures are first analyzed using powder X-ray diffraction (PXRD), where the (111) and (300) planes at 10.8 and 18.8° are observed, and the original structures of MBTC are retained after secondary growth (Figure 2a). The Raman tests show a reduced signal at 81.0 cm^{-1} for ZnCoBTC compared with pure CoBTC, verifying partial substitution by ZnBTC (Figure 2b). Meanwhile, the benzene and carboxylate vibrations of BTC^{3-} are attributed to 3700−3300 and 1700−1300 cm^{-1} in the FT-IR spectra, respectively, with one weak signal at 3233.9 cm^{-1} from the terminally coordinated hydroxide (Figure 2c). It is worth mentioning that the two sharp peaks at 1600 and 1710 cm^{-1} correspond to the stretching vibrations of the C═C bond in the benzene ring and the C═O bond in the carboxylate groups, respectively. To expose more catalytic sites, large-particle CoBTC could be electrochemically degraded into the CoO_xH_y species with two obvious oxidation peaks at 1.11−1.13 and 1.45−1.48 V (Figures 2d, S6, and S7). For CoZnBTC, the oxidation peak positively shifts to 1.15−1.21 V due to the presence of Zn, limiting the oxidation of Co species (Figures 2e and S8a−c). The situation in ZnCoBTC is almost the same as that in CoBTC (1.08−1.15 V, Figures 2f and S8d−f). During electrolysis, the conversion position of Co(III) to Co(IV) does not change significantly in the three materials, and ZnO_xH_y could not be generated owing to the rapid dissolution of ZnBTC. The corresponding SEM images of the three electrolysis products are depicted in Figure 2g−i. The obtained CoO_xH_y exhibits binary hexagonal nanosheets consistent with previous reports,[45,46] but $CoZnO_xH_y$ reveals a disordered 2D structure with a slight tendency to form a

https://doi.org/10.1021/acs.inorgchem.3c02210
Inorg. Chem. 2023, 62, 14757−14763

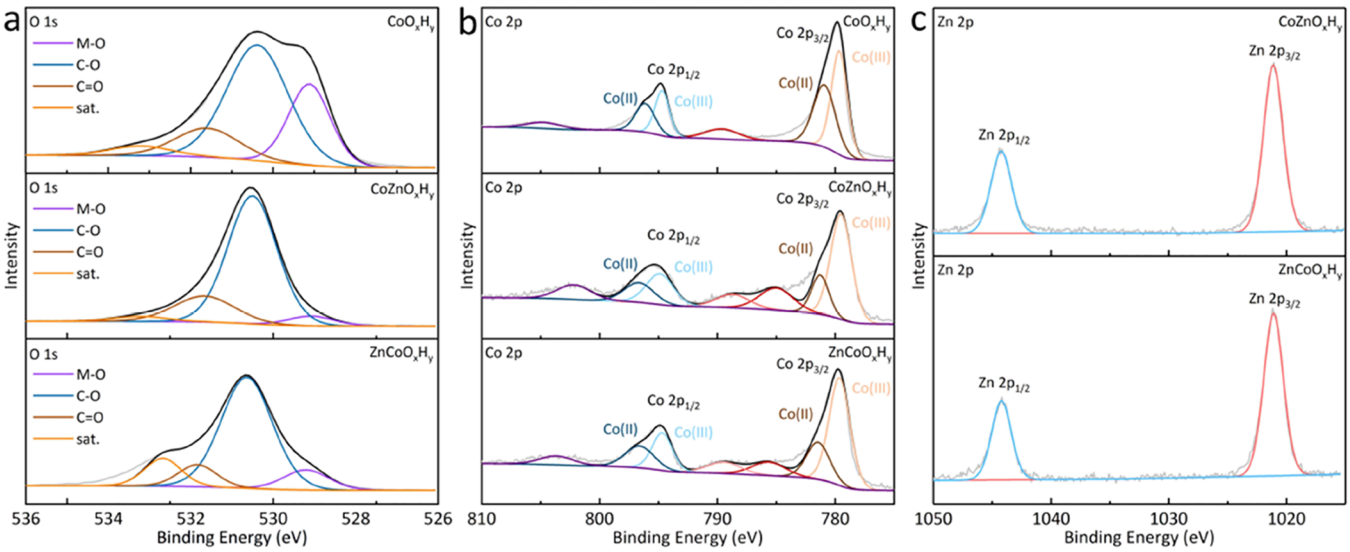

Figure 4. Deconvoluted XPS spectra of (a) O 1s, (b) Co 2p, and (c) Zn 2p for CoO_xH_y, $CoZnO_xH_y$, and $ZnCoO_xH_y$.

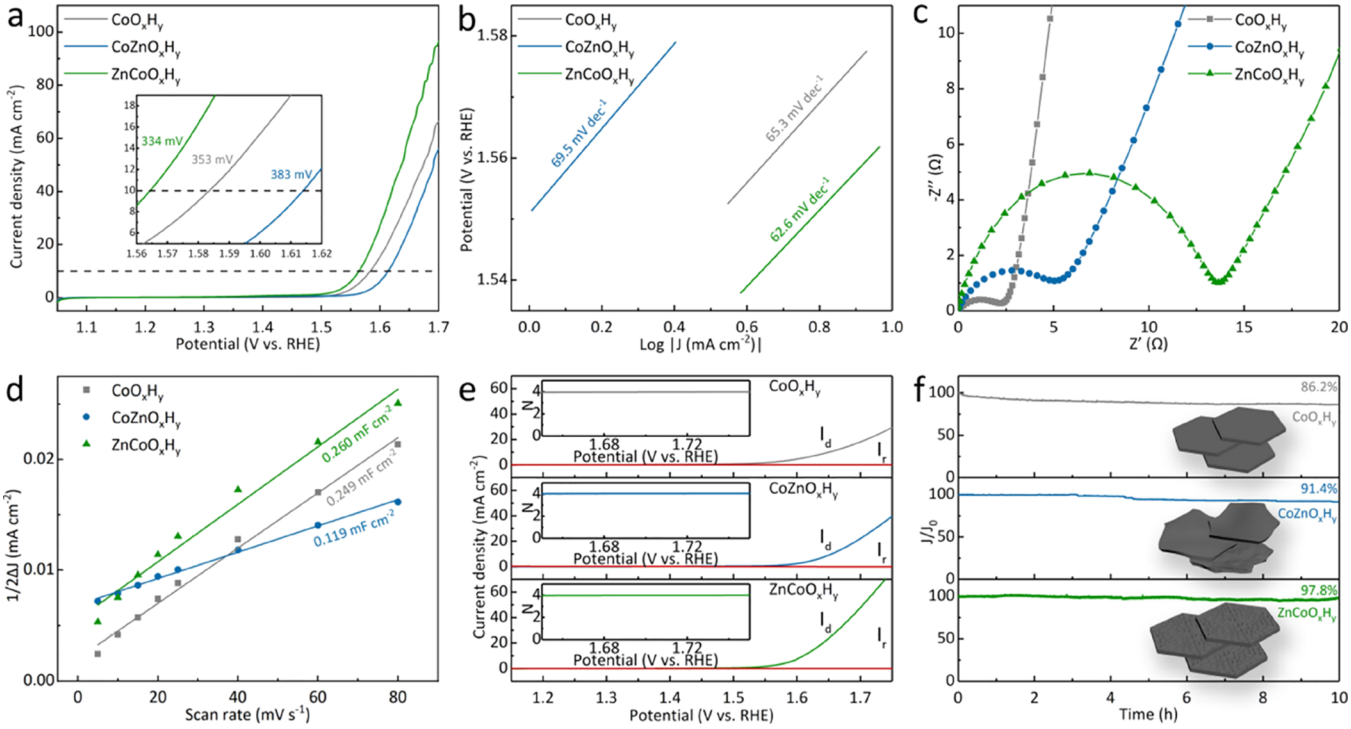

Figure 5. (a) Polarization curves; (b) Tafel plots; (c) EIS spectra; (d) linear fitting of C_{dl} with different scan rates; (e) RRDE voltammogram, and its inset shows the electron-transfer number; and (f) i-t curves.

hexagonal structure because Zn sites are easily dissolved (Figures 2g,h and S9a−d). The electrolysis product of ZnCoBTC maintains a hexagonal structure, and its morphological defects expose abundant active sites that would further improve the electrochemical performance (Figures 2i and S9e,f).

The absence of clear diffraction peaks in the degradation products indicates complete decomposition of the precursors (Figure 3a). In Figure 3b, the reduced characteristic peak at 693 cm^{-1} in Raman spectra suggests fewer CoO_xH_y species in ZnCoBTC and CoZnBTC than in CoBTC. The coexisting peaks at 181 and 450−550 cm^{-1} exhibit $Co(OH)_2$ and CoOOH as the main substances in the electrolyzed product. The weak FT-IR peaks at 412−480 cm^{-1} in Figure 3c indicate a small amount of residual Zn-based species, and Co−O peaks are observed at 845−583 cm^{-1} for all samples, suggesting the presence of generated metal oxide/hydroxide. The hexagonal nanosheets with lattice fringes of 0.47 and 0.28 nm to the (001) plane of $Co(OH)_2$ and (130) plane of CoOOH, respectively, are revealed, while the defective hexagonal $CoZnO_xH_y$ with numerous small particles of active species is shown in Figure 3d,e. The lattice fringes of CoOOH (0.23 nm) correspond to the (111) crystal plane, which is also accompanied by a blurred (211) crystal plane of 0.25 nm for ZnO_xH_y. For $ZnCoO_xH_y$, its TEM image and EDS analysis show a low Zn content, indicative of its complete dissolution,

https://doi.org/10.1021/acs.inorgchem.3c02210
Inorg. Chem. 2023, 62, 14757−14763

resulting in more Co active sites and noticeable particles on the surface (Figures 3f and S10). Similarly, lattice fringes correspond only to the (121) plane of CoOOH (0.21 nm) and the (001) plane of $Co(OH)_2$ (0.47 nm). Element mapping in Figure S11 shows that the content of Zn significantly affects the final morphological characteristics of the electrolyzed materials.

It is further employed to investigate the chemical states in these MOF derivatives by X-ray photoelectron spectroscopy (XPS, Figure S12). The deconvoluted O 1s spectra reveal a predominant C−O peak at ∼530.5 eV in Figure 4a, along with two other peaks at 529.1 and 532.5 eV corresponding to M−O and C═O, respectively. The M−O peak position shows no shift to indicate that the dissolution of Zn does not affect the coordination between Co and O. Figure S13 exhibits a shift in the C 1s peak position of CoO_xH_y compared to $CoZnO_xH_y$ and $ZnCoO_xH_y$, suggesting that the coordination environment of C species could be disrupted. The two higher peaks at 292.4 and 295.2 eV correspond to the C−K bond to verify the effect of KOH during the degradation process.[47,48] The deconvoluted N 1s spectra are almost indistinguishable and mainly come from the N,N-Dimethylformamide (DMF) solvent (Figure S14). Figure 4b shows that Co(II) $2p_{3/2}$ at 781.0 eV and Co(II) $2p_{1/2}$ at 796.2 eV originate from $Co(OH)_2$, and another pair of peaks at 779.7 and 794.7 eV are assigned to Co(III) $2p_{3/2}$ and $2p_{1/2}$, respectively. The presence of Zn in $CoZnO_xH_y$ and $ZnCoO_xH_y$ results in a higher binding energy of Co(II), making it easier for electrons to be biased toward Zn. Clearly, a small amount of Zn in $ZnCoO_xH_y$ also affects the coordination environment of Co, but it remains almost unchanged with $CoZnO_xH_y$. The shift in the peak position in the Zn 2p spectra in Figure 4c also corresponds to this phenomenon. The XPS data support the speculation that the presence of heterometals in the original MOFs could adjust the coordination environment of various elements, resulting in the exposure of more active materials for electrochemical performance improvement (Table S4).

The OER performance is first evaluated in Figure 5a, and the LSV curve of $ZnCoO_xH_y$ presents the best OER activity, requiring only an overpotential of 334 mV to reach 10 mA cm^{-2}, which is lower than those of $CoZnO_xH_y$ (383 mV) and CoO_xH_y (353 mV). In Figure 5b, the Tafel slopes of the three materials are relatively close, with CoO_xH_y at 65.3 mV dec^{-1}, $CoZnO_xH_y$ at 69.5 mV dec^{-1}, and $ZnCoO_xH_y$ at 62.6 mV dec^{-1}. Furthermore, electrochemical impedance spectroscopy (EIS) reveals that CoO_xH_y has the lowest charge transfer resistance of about 2.41 Ω in alkaline, attributable to its well-preserved hexagonal morphology (Figure 5c). In this case, $ZnCoO_xH_y$ and $CoZnO_xH_y$ have defects caused by Zn species with higher resistance, but the difference in the value is not significant. The double-layer capacitances (C_{dl}) of CoO_xH_y, $CoZnO_xH_y$, and $ZnCoO_xH_y$ are calculated to be 0.249, 0.119, and 0.260 mF cm^{-2}, respectively, further proving that defects reduce the electrochemically active surface area and expose more active materials (Figures 5d and S15). To evaluate the reaction mechanism, the RRDE electrode is further used to calculate the electron-transfer number (N), with the ring current (I_r) being almost negligible compared to the disk current (I_d), demonstrating its high selectivity for the four-electron process (Figure 5e). In Figure 5f, the long-term stability of the electrolyzed electrocatalysts is evaluated to give a 97.8% current density retention through a 10 h i-t test for $ZnCoO_xH_y$, indicative of its satisfactory stability of catalytic OER activity. CoO_xH_y and $CoZnO_xH_y$ also demonstrate moderate stability, indicating that defects introduced by Zn not only increase the exposure of active materials but also prevent the loss of active materials, improving the long-term stability of these materials.

■ CONCLUSIONS

In conclusion, this study presents an approach for designing and synthesizing heterometallic ZnCo-MOF precursors using transition metals with the same coordination environment. Under continuous electrolysis, these precursors can be easily converted to ultrathin nanomaterials with synergistic metal sites and structural defects. Specifically, the study demonstrated that pure CoBTC could be transformed into ultrathin hexagonal CoO_xH_y nanosheets, while the conversion of ZnCoBTC into $ZnCoO_xH_y$ with abundant active sites of different valence states achieved efficient OER. The optimal $ZnCoO_xH_y$ required an ultrasmall η_{10} value (334 mV), much smaller than its control samples, with satisfactory stability, indicating its potential as an efficient electrocatalyst for practical applications. The approach demonstrated in this work can be extended to designing other MOFs and their derivatives, offering a promising strategy for developing efficient and cost-effective electrocatalysts for the transition to a sustainable energy future.

■ ASSOCIATED CONTENT

Supporting Information

The Supporting Information is available free of charge at https://pubs.acs.org/doi/10.1021/acs.inorgchem.3c02210.

Experimental material characterizations; electrochemical measurement and method; SEM/TEM images; PXRD patterns, FT-IR spectra, thermogravimetric analysis (TGA) data, and XPS curves of control samples; and additional electrochemical test (PDF)

■ AUTHOR INFORMATION

Corresponding Author

Jinjie Qian − *Key Laboratory of Carbon Materials of Zhejiang Province, College of Chemistry and Materials Engineering, Wenzhou University, Wenzhou, Zhejiang 325000, P. R. China*; orcid.org/0000-0002-9996-7929; Email: jinjieqian@wzu.edu.cn

Authors

Shaojie Xu − *Key Laboratory of Carbon Materials of Zhejiang Province, College of Chemistry and Materials Engineering, Wenzhou University, Wenzhou, Zhejiang 325000, P. R. China*

Huijie Ni − *Key Laboratory of Carbon Materials of Zhejiang Province, College of Chemistry and Materials Engineering, Wenzhou University, Wenzhou, Zhejiang 325000, P. R. China*

Xiaodeng Zhang − *Key Laboratory of Carbon Materials of Zhejiang Province, College of Chemistry and Materials Engineering, Wenzhou University, Wenzhou, Zhejiang 325000, P. R. China*

Cheng Han − *Key Laboratory of Carbon Materials of Zhejiang Province, College of Chemistry and Materials Engineering, Wenzhou University, Wenzhou, Zhejiang 325000, P. R. China*

Complete contact information is available at:

https://doi.org/10.1021/acs.inorgchem.3c02210
Inorg. Chem. 2023, 62, 14757−14763

https://pubs.acs.org/10.1021/acs.inorgchem.3c02210

Author Contributions

J.Q. conceived the research project. S.X., X.Z., and C.H. conducted the experiments, performed the characterizations, and wrote the manuscript. S.X. revised the main article. All authors have checked and given approval to the final version of the manuscript.

Notes

The authors declare no competing financial interest.

■ ACKNOWLEDGMENTS

This work was financially supported by the National Natural Science Foundation of China (21601137), Natural Science Foundation of Zhejiang Province (LQ16B010003), Basic Science and Technology Research Project of Wenzhou, Zhejiang Province (H20220001), and the Special Basic Cooperative Research Programs of Yunnan Provincial Undergraduate Universities Association (202101BA070001-042).

■ REFERENCES

(1) Georgeson, L.; Maslin, M.; Poessinouw, M. Clean up Energy Innovation. *Nature* **2016**, *538* (7623), 27−29.

(2) Huang, K. J.; Li, L.; Olivetti, E. A. Designing for Manufacturing Scalability in Clean Energy Research. *Joule* **2018**, *2* (9), 1642−1647.

(3) Qi, J.; Zhang, W.; Cao, R. Solar-to-Hydrogen Energy Conversion Based on Water Splitting. *Adv. Energy Mater.* **2018**, *8* (5), No. 1701620.

(4) Hermesmann, M.; Müller, T. E. Green, Turquoise, Blue, or Grey? Environmentally Friendly Hydrogen Production in Transforming Energy Systems. *Prog. Energy Combust. Sci.* **2022**, *90*, No. 100996.

(5) Carroll, G. M.; Gebbie, M. A.; Stahl, S. S.; Johnson, M. R.; Luca, O. R.; Petersen, H. A.; Bomble, Y. J.; Neale, N. R.; Cortright, R. D. Alternative Energy Carriers: Unique Interfaces for Electrochemical Hydrogenic Transformations. *Adv. Energy Mater.* **2023**, *13* (14), No. 2203751.

(6) Dincer, I.; Aydin, M. I. New Paradigms in Sustainable Energy Systems with Hydrogen. *Energy Convers. Manage.* **2023**, *283*, No. 116950.

(7) Wang, X.; Huang, H.; Qian, J.; Li, Y.; Shen, K. Intensified Kirkendall Effect Assisted Construction of Double-Shell Hollow Cu-Doped CoP Nanoparticles Anchored by Carbon Arrays for Water Splitting. *Appl. Catal. B: Environ.* **2023**, *325*, No. 122295.

(8) Wang, X.; Zhong, H.; Xi, S.; Lee, W. S. V.; Xue, J. Understanding of Oxygen Redox in the Oxygen Evolution Reaction. *Adv. Mater.* **2022**, *34* (50), No. 2107956.

(9) Liu, S.; Liu, M.; Li, X.; Yang, S.; Miao, Q.; Xu, Q.; Zeng, G. Metal Organic Polymers with Dual Catalytic Sites for Oxygen Reduction and Oxygen Evolution Reactions. *Carbon Energy* **2023**, *5*, No. e303.

(10) Lyu, F.; Wang, Q.; Choi, S. M.; Yin, Y. Noble-Metal-Free Electrocatalysts for Oxygen Evolution. *Small* **2019**, *15* (1), No. 1804201.

(11) Zhang, H.; Shi, P.; Ma, X.; Ma, C.; Han, S.; He, C.; Wu, H.; Zhu, L.; Zhang, B.; Lu, Y.; Cao, W.; Yin, H.; Meng, X.; Xia, J.; Zhang, J.; Wang, A.; Lu, Q. Construction of Ordered Atomic Donor−Acceptor Architectures in Bcc IrGa Intermetallic Compounds toward Highly Electroactive and Stable Overall Water Splitting. *Adv. Energy Mater.* **2023**, *13* (1), No. 2202703.

(12) Chen, D.; Sun, Q.; Han, C.; Guo, Y.; Huang, Q.; Goddard, W. A.; Qian, J. Enhanced Oxygen Evolution Catalyzed by *in Situ* Formed Fe-Doped Ni Oxyhydroxides in Carbon Nanotubes. *J. Mater. Chem. A* **2022**, *10* (30), 16007−16015.

(13) Huang, Q.; Yang, Y.; Qian, J. Structure-Directed Growth and Morphology of Multifunctional Metal-Organic Frameworks. *Coord. Chem. Rev.* **2023**, *484*, No. 215101.

(14) Li, S.; Gao, Y.; Li, N.; Ge, L.; Bu, X.; Feng, P. Transition Metal-Based Bimetallic MOFs and MOF-Derived Catalysts for Electrochemical Oxygen Evolution Reaction. *Energy Environ. Sci.* **2021**, *14* (4), 1897−1927.

(15) Hong, Q.; Wang, Y.; Wang, R.; Chen, Z.; Yang, H.; Yu, K.; Liu, Y.; Huang, H.; Kang, Z.; Menezes, P. W. In Situ Coupling of Carbon Dots with Co-ZIF Nanoarrays Enabling Highly Efficient Oxygen Evolution Electrocatalysis. *Small* **2023**, *19*, No. 2206723.

(16) Wu, H.; Li, Z.; Wang, Z.; Ma, Y.; Huang, S.; Ding, F.; Li, F.; Zhai, Q.; Ren, Y.; Zheng, X.; Yang, Y.; Tang, S.; Deng, Y.; Meng, X. Regulation of Electronic Structure in Medium-Entropy Metal Sulfides Nanoparticles as Highly Efficient Bifunctional Electrocatalysts for Zinc-Air Battery. *Appl. Catal. B: Environ.* **2023**, *325*, No. 122356.

(17) Daglar, H.; Gulbalkan, H. C.; Avci, G.; Aksu, G. O.; Altundal, O. F.; Altintas, C.; Erucar, I.; Keskin, S. Effect of Metal−Organic Framework (MOF) Database Selection on the Assessment of Gas Storage and Separation Potentials of MOFs. *Angew. Chem., Int. Ed.* **2021**, *60* (14), 7828−7837.

(18) Hai, G.; Wang, H. Theoretical Studies of Metal-Organic Frameworks: Calculation Methods and Applications in Catalysis, Gas Separation, and Energy Storage. *Coord. Chem. Rev.* **2022**, *469*, No. 214670.

(19) Mon, M.; Bruno, R.; Ferrando-Soria, J.; Bartella, L.; Di Donna, L.; Talia, M.; Lappano, R.; Maggiolini, M.; Armentano, D.; Pardo, E. Crystallographic Snapshots of Host−Guest Interactions in Drugs@metal−Organic Frameworks: Towards Mimicking Molecular Recognition Processes. *Mater. Horiz.* **2018**, *5* (4), 683−690.

(20) Liu, L.; Ru, L.; Tang, H.; Zhang, Z.; Feng, W. A Multi-Responsive Tb-Doped MOF Probe for Highly Specific Breath Volatile Biomarker Recognition of Lung Cancer. *J. Mater. Chem. C* **2023**, *11* (8), 3059−3069.

(21) Han, C.; Zhang, X.; Huang, S.; Hu, Y.; Yang, Z.; Li, T.; Li, Q.; Qian, J. MOF-on-MOF-Derived Hollow Co_3O_4/In_2O_3 Nanostructure for Efficient Photocatalytic CO_2 Reduction. *Adv. Sci.* **2023**, *10*, No. 2300797.

(22) Qian, Z.; Zhang, R.; Xiao, Y.; Huang, H.; Sun, Y.; Chen, Y.; Ma, T.; Sun, X. Trace to the Source: Self-Tuning of MOF Photocatalysts. *Adv. Energy Mater.* **2023**, *13*, No. 2300086.

(23) Xia, J.; Wang, B.; Di, J.; Li, Y.; Yang, S.-Z.; Li, H.; Guo, S. Construction of Single-Atom Catalysts for Electro-, Photo- and Photoelectro-Catalytic Applications: State-of-the-Art, Opportunities, and Challenges. *Mater. Today* **2022**, *53*, 217−237.

(24) He, Y.; Yin, Z.; Wang, Z.; Wang, H.; Xiong, W.; Song, B.; Qin, H.; Xu, P.; Zeng, G. Metal-Organic Frameworks as a Good Platform for the Fabrication of Multi-Metal Nanomaterials: Design Strategies, Electrocatalytic Applications and Prospective. *Adv. Colloid Interface Sci.* **2022**, *304*, No. 102668.

(25) Castillo-Blas, C.; Álvarez-Galván, C.; Puente-Orench, I.; García-Sánchez, A.; Oropeza, F. E.; Gutiérrez-Puebla, E.; Monge, Á.; De La Peña-O'Shea, V. A.; Gándara, F. Highly Efficient Multi-Metal Catalysts for Carbon Dioxide Reduction Prepared from Atomically Sequenced Metal Organic Frameworks. *Nano Res.* **2021**, *14* (2), 493−500.

(26) De Villenoisy, T.; Zheng, X.; Wong, V.; Mofarah, S. S.; Arandiyan, H.; Yamauchi, Y.; Koshy, P.; Sorrell, C. C. Principles of Design and Synthesis of Metal Derivatives from MOFs. *Adv. Mater.* **2023**, *35*, No. 2210166.

(27) Zhao, T.; Wu, H.; Wen, X.; Zhang, J.; Tang, H.; Deng, Y.; Liao, S.; Tian, X. Recent Advances in MOFs/MOF Derived Nanomaterials toward High-Efficiency Aqueous Zinc Ion Batteries. *Coord. Chem. Rev.* **2022**, *468*, No. 214642.

(28) Wang, Y.-L.; Yang, S.-H.; Wang, H.-Y.; Wang, G.-S.; Sun, X.-B.; Yin, P.-G. Hollow Porous CoNi/C Composite Nanomaterials Derived from MOFs for Efficient and Lightweight Electromagnetic Wave Absorber. *Carbon* **2020**, *167*, 485−494.

(29) Oveisi, M.; Asli, M. A.; Mahmoodi, N. M. MIL-Ti Metal-Organic Frameworks (MOFs) Nanomaterials as Superior Adsorbents: Synthesis and Ultrasound-Aided Dye Adsorption from Multi-

component Wastewater Systems. *J. Hazard. Mater.* **2018**, *347*, 123−140.

(30) Wu, Y.; Chen, L.; Yang, X.; Li, Y.; Shen, K. Facet-Selective Growth of MOF-on-MOF Heterostructures Enables Etching-Free Synthesis of Highly-Open Co/N-Doped Carbon Nanoframes for Efficient Catalysis. *Sci. China Chem.* **2022**, *65* (12), 2450−2461.

(31) Wang, Z.; Shen, K.; Chen, L.; Li, Y. Scalable Synthesis of Multi-Shelled Hollow N-Doped Carbon Nanosheet Arrays with Confined Co/CoP Heterostructures from MOFs for PH-Universal Hydrogen Evolution Reaction. *Sci. China Chem.* **2022**, *65* (3), 619−629.

(32) He, Y.; Yin, Z.; Wang, Z.; Wang, H.; Xiong, W.; Song, B.; Qin, H.; Xu, P.; Zeng, G. Recent Progress on Mixed Transition Metal Nanomaterials Based on Metal−Organic Frameworks for Energy-Related Applications. *J. Mater. Chem. A* **2022**, *10* (18), 9788−9820.

(33) Han, C.; Zhang, X.; Sun, Q.; Chen, D.; Miao, T.; Su, K.; Li, Q.; Huang, S.; Qian, J. Phthalocyanine-Induced Iron Active Species in Metal−Organic Framework-Derived Porous Carbon for Efficient Alkaline Zinc−Air Batteries. *Inorg. Chem. Front.* **2022**, *9* (11), 2557−2567.

(34) Wang, H.; Gu, M.; Huang, X.; Gao, A.; Liu, X.; Sun, P.; Zhang, X. Ligand-Based Modulation of the Electronic Structure at Metal Nodes in MOFs to Promote the Oxygen Evolution Reaction. *J. Mater. Chem. A* **2023**, *11* (13), 7239−7245.

(35) Wu, Y.; Wang, L.; Chen, L.; Li, Y.; Shen, K. Morphology-Engineering Construction of Anti-Aggregated Co/N-Doped Hollow Carbon from Metal-Organic Frameworks for Efficient Biomass Upgrading. *Small* **2023**, *19* (20), No. 2207689.

(36) Ao, K.; Wei, Q.; Daoud, W. A. MOF-Derived Sulfide-Based Electrocatalyst and Scaffold for Boosted Hydrogen Production. *ACS Appl. Mater. Interfaces* **2020**, *12* (30), 33595−33602.

(37) Hu, S.; Wang, S.; Feng, C.; Wu, H.; Zhang, J.; Mei, H. Novel MOF-Derived Nickel Nitride as High-Performance Bifunctional Electrocatalysts for Hydrogen Evolution and Urea Oxidation. *ACS Sustainable Chem. Eng.* **2020**, *8* (19), 7414−7422.

(38) Bhanja, P.; Kim, Y.; Paul, B.; Lin, J.; Alshehri, S. M.; Ahamad, T.; Kaneti, Y. V.; Bhaumik, A.; Yamauchi, Y. Facile Synthesis of Nanoporous Transition Metal-Based Phosphates for Oxygen Evolution Reaction. *ChemCatChem.* **2020**, *12* (7), 2091−2096.

(39) Guo, Y.; Zhang, C.; Zhang, J.; Dastafkan, K.; Wang, K.; Zhao, C.; Shi, Z. Metal−Organic Framework-Derived Bimetallic NiFe Selenide Electrocatalysts with Multiple Phases for Efficient Oxygen Evolution Reaction. *ACS Sustainable Chem. Eng.* **2021**, *9* (5), 2047−2056.

(40) Bhanja, P.; Kim, Y.; Paul, B.; Kaneti, Y. V.; Alothman, A. A.; Bhaumik, A.; Yamauchi, Y. Microporous Nickel Phosphonate Derived Heteroatom Doped Nickel Oxide and Nickel Phosphide: Efficient Electrocatalysts for Oxygen Evolution Reaction. *Chem. Eng. J.* **2021**, *405*, No. 126803.

(41) Septiani, N. L. W.; Kaneti, Y. V.; Guo, Y.; Yuliarto, B.; Jiang, X.; Ide, Y.; Nugraha, N.; Dipojono, H. K.; Yu, A.; Sugahara, Y.; Golberg, D.; Yamauchi, Y. Holey Assembly of Two-Dimensional Iron-Doped Nickel-Cobalt Layered Double Hydroxide Nanosheets for Energy Conversion Application. *ChemSusChem* **2020**, *13* (6), 1645−1655.

(42) Chai, L.; Pan, J.; Hu, Y.; Qian, J.; Hong, M. Rational Design and Growth of MOF-on-MOF Heterostructures. *Small* **2021**, *17* (36), No. 2100607.

(43) Li, Y.; Han, W.; Wang, R.; Weng, L.-T.; Serrano-Lotina, A.; Bañares, M. A.; Wang, Q.; Yeung, K. L. Performance of an Aliovalent-Substituted CoCeOx Catalyst from Bimetallic MOF for VOC Oxidation in Air. *Appl. Catal. B: Environ.* **2020**, *275*, No. 119121.

(44) Gu, Y.; Wu, Y.; Li, L.; Chen, W.; Li, F.; Kitagawa, S. Controllable Modular Growth of Hierarchical MOF-on-MOF Architectures. *Angew. Chem., Int. Ed.* **2017**, *56* (49), 15658−15662.

(45) Zhong, R.; Wu, P.; Wang, Q.; Zhang, X.; Du, L.; Liu, Y.; Yang, H.; Gu, M.; Zhang, Z. C.; Huang, L.; Ye, S. Room-Temperature Fabrication of Defective CoO_xH_y Nanosheets with Abundant Oxygen Vacancies and High Porosity as Efficient 5-Hydroxymethylfurfural Oxidation Electrocatalysts. *Green Chem.* **2023**, *25*, 4674−4684, DOI: 10.1039/D3GC00588G.

(46) Lopes, P. P.; Chung, D. Y.; Rui, X.; Zheng, H.; He, H.; Farinazzo Bergamo Dias Martins, P.; Strmcnik, D.; Stamenkovic, V. R.; Zapol, P.; Mitchell, J. F.; Klie, R. F.; Markovic, N. M. Dynamically Stable Active Sites from Surface Evolution of Perovskite Materials during the Oxygen Evolution Reaction. *J. Am. Chem. Soc.* **2021**, *143* (7), 2741−2750.

(47) Diaz-Terán, J.; Nevskaia, D. M.; Fierro, J. L. G.; López-Peinado, A. J.; Jerez, A. Study of Chemical Activation Process of a Lignocellulosic Material with KOH by XPS and XRD. *Microporous Mesoporous Mater.* **2003**, *60* ((1−3)), 173−181.

(48) Elmouwahidi, A.; Bailón-García, E.; Pérez-Cadenas, A. F.; Maldonado-Hódar, F. J.; Carrasco-Marín, F. Activated Carbons from KOH and H 3 PO 4 -Activation of Olive Residues and Its Application as Supercapacitor Electrodes. *Electrochim. Acta* **2017**, *229*, 219−228.